Dominant *s*-wave superconducting gap in $PdTe_2$ observed by tunneling spectroscopy on side junctions

J. A. Voerman,[1,*] J. C. de Boer,[1,*] T. Hashimoto,[1,2] Yingkai Huang,[3] Chuan Li,[1] and A. Brinkman[1]

[1]*MESA+ Institute for Nanotechnology, University of Twente, 7500 AE Enschede, The Netherlands*

[2]*Yukawa Institute for Theoretical Physics, Kyoto University, Kyoto 606-8502, Japan*

[3]*Van der Waals-Zeeman Institute, University of Amsterdam, Science Park 904, 1098 XH Amsterdam, The Netherlands*

(Received 12 October 2018; revised manuscript received 22 November 2018; published 11 January 2019)

We have fabricated superconductor-normal metal side junctions with different barrier transparencies out of $PdTe_2$ crystalline flakes and measured the differential conductance spectra. Modeling our measurements using a modified Blonder, Tinkham, and Klapwijk (BTK) formalism confirms that the superconductivity is mostly comprised of the conventional *s*-wave symmetry. We have found that for junctions with very low barrier transparencies, the junctions can enter a thermal regime, where the critical current becomes important. Adding this to the BTK model allows us to accurately fit the experimental data, from which we conclude that the superconductivity in the *a*-*b* plane of $PdTe_2$ is dominated by conventional *s*-wave pairing.

DOI: 10.1103/PhysRevB.99.014510

I. INTRODUCTION

The search for the elusive Majorana particle has brought physicists to the area of topological superconductivity. The mixture of Dirac physics and superconductivity (SC) is seen as a promising way of creating Majorana quasiparticles [1], which in turn opens up the possibility of quantum computing through a process called braiding [2]. Experimental research has focused on the interface effects of superconductors coupled to either semiconductors with strong spin-orbit coupling [3,4] or topological matter [5–8]. Topological superconductors, for example $Cu_xBi_2Se_3$, are also studied in the context of Majorana physics [9,10]. The transition-metal dichalcogenide $PdTe_2$ belongs to the $P\bar{3}m1$ space group and is known to be a superconductor [11–13]. Recent experiments have shown that this material is also topological as it possesses a type-II Dirac cone [14–16], highlighting it as an extraordinary material, that could host unconventional superconductivity intrinsically [17]. Notably, Teknowijoyo *et al.* have narrowed the possible order parameter (OP) symmetries down to three candidates: A_{1g} (conventional *s*-wave) pairing, A_{1u} (helical *p*-wave) pairing, or $E_{u(1,0)}$ (nematic $p+f$-wave) pairing, by showing that the order parameter of $PdTe_2$ is nodeless [18]. The latter two pairings are nontrivial. Experiments investigating the nature of the superconductivity in $PdTe_2$ have so far found no indication of unconventional superconductivity [12].

In this paper we present tunneling spectroscopy measurements performed on $PdTe_2$–normal metal side junctions, to shed light on the in-plane properties of the order parameter and distinguish between the three possible OPs that Teknowijoyo *et al.* have singled out. We model the data using a combination of the Blonder, Tinkham, and Klapwijk (BTK) formalism [19] and the effect of the critical current, I_c, on the differential conductance [20–24]. Finally we show additional features found in the dI/dV spectrum of the purely ballistic junction, together with an analysis of these features that are beyond our BTK and I_c model.

II. EXPERIMENTAL DETAILS

We have fabricated our superconductor–(insulator–)normal metal [S(I)N] junctions out of exfoliated flakes of a $PdTe_2$ crystal. The crystal has a preferred cleavage plane, which orientates all flakes with the *c* axis out of plane. The single crystal of $PdTe_2$ was grown by a modified Bridgman method. High-purity Pd (99.99%) and Te (99.9999%) were used as starting materials. The desired components were sealed in an evacuated cone-ended quartz ampoule. The ampoule was heated up to 800 °C, kept for 48 h, and then cooled down to 500 °C at a rate of 3 °C/h, followed by furnace cooling.

All devices are prepared by Ar^+ milling through the flake prior to the deposition of a barrier and normal metal, in order to create a side contact, allowing us to probe the in-plane properties of the superconducting order parameter. All patterning for these steps was done using standard electron-beam lithography. The devices differ in their interfaces between the $PdTe_2$ and the normal metal. The first type of device was made without a specific barrier and is a 500-nm-wide SN interface between $PdTe_2$ and gold, with a normal state resistance (R_N) of about 30 Ω at 15 mK. The second type of device was made by transferring the argon milled flakes to a sputter machine where they were cleaned of contaminations by low rf power plasma etching. On the cleaned surface, 1 nm of Al was sputter deposited, followed by oxidiation in 10 mbar of oxygen for 1 h to form an Al_2O_3 oxide barrier. To finalize the devices, a normal metal layer of palladium was sputter deposited on the aluminum oxide without breaking the vacuum. The R_N was about 200 Ω at 15 mK. Of the third type of devices only one was fabricated. This device was transferred to an atomic layer deposition apparatus after argon milling, where a 1.2-nm-thick Al_2O_3 layer was grown

[*]These two authors contributed equally to this work.

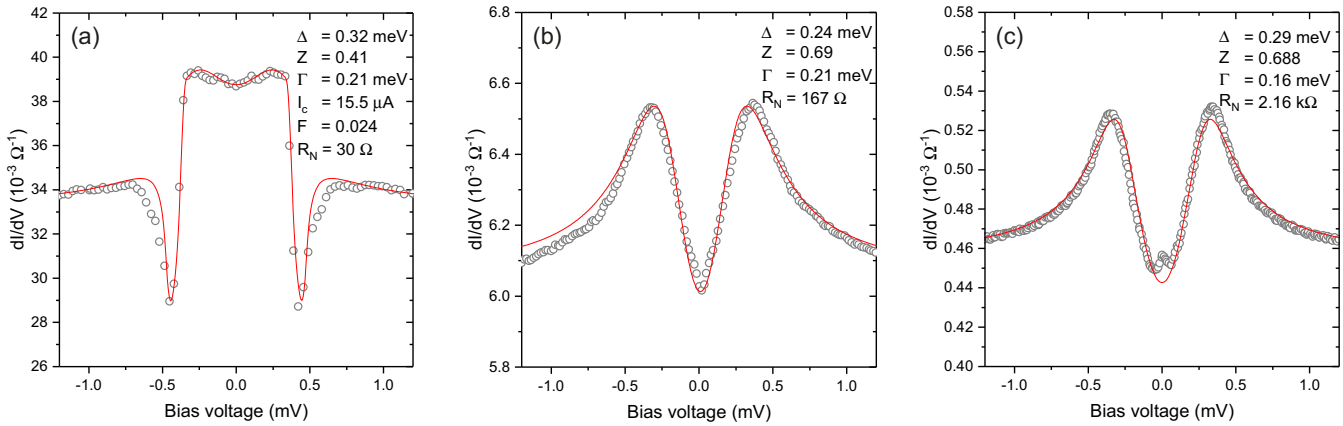

FIG. 1. dI/dV spectra of three $PdTe_2$ junctions with different resistances measured at base temperature (gray circles). The red line is our best fit to the data. All relevant fitting parameters, as well as R_N, are included in the panel. (a) dI/dV measurements and fit of a BTK model with a very transparent $PdTe_2$/Au interface ($R_N = 30\ \Omega$) and critical current effects. (b) dI/dV measurements and fit of a BTK model with a slightly less transparent $PdTe_2/Al_2O_3$/Pd interface ($R_N = 167\ \Omega$). (c) dI/dV measurements and fit of a BTK model with an opaque $PdTe_2/Al_2O_3$/Au interface ($R_N = 2.16\ \text{k}\Omega$).

at 100 °C, followed by *ex situ* deposition of 40 nm of gold by sputter deposition. These SIN junctions have an R_N of about 2 kΩ at 15 mK. Although many junctions were made, one SIN junction had this resistance value at base temperature, whereas the other showed $R > 1$ MΩ. Several of our similarly fabricated SIS junctions did show an R_N of 2 kΩ at 15 mK, but are not included in this work on SIN junctions. For each of the three S(I)N types, measurements on one representative device are presented in this work.

III. RESULTS AND ANALYSIS

We drive a dc bias current with a small ac excitation through the junctions while measuring both the dc and ac response across the junction to probe the differential resistance. The measured differential resistance is numerically inverted to differential conductance and plotted against the measured dc bias voltage. The results of these measurements at the lowest temperature reached ($T < 100$ mK) are shown as gray circles in Fig. 1. Comparing the three graphs we see a clear evolution of the main feature around zero bias. In Fig. 1(a) we see a dented plateau around zero bias, accompanied by sharp dips in conductance at ±0.5 mV. Figure 1(b) shows a quite different shape. The dented plateau around zero has been replaced by an Andreev-like spectrum with coherence peaks surrounding a clear dip. The final device, whose differential conductance is shown in Fig. 1(c), has the highest normal state resistance. Just as the data in Fig. 1(b), the measured dI/dV spectrum in Fig. 1(c) looks like a clear Andreev spectrum. Around zero bias a small zero-bias conductance peak (ZBCP) is visible.

Because our $PdTe_2$ flakes are less than 100 nm thick, which is less than the reported superconducting coherence length [11,18], we have modeled the conductance spectra numerically using a two-dimensional (2D) BTK formalism for different order parameters. In this model, the bands are assumed to be parabolic since the Fermi energy is much larger than the energy where the type-II Dirac points reside [16]. The chemical potential mismatch, μ_{sc}/μ_n, is set to 1 for simplicity, so that $Z = Hm_e/\hbar^2 k_{sc}$, with H the height of the δ-shaped barrier, is the only barrier parameter. Teknowijoyo *et al.* have experimentally determined the OP in $PdTe_2$ to be nodeless, which, together with crystal symmetry constraints, leaves us with three different pair potentials: A_{1g} (conventional s-wave), A_{1u} (helical p-wave), and $E_{u(1,0)}$ (nematic $p + f$-wave). The latter two correspond to the d vectors $\mathbf{d}_{A_{1u}} = k_x\hat{x} + k_y\hat{y} + k_z\hat{z}$ and $\mathbf{d}_{E_{u(1,0)}} = k_x(k_x^2 - 3k_y^2)\hat{x} + k_z\hat{y} + k_y\hat{z}$. Before moving on to fitting our measured conductance spectra, we show the general features of the three OPs in a 2D BTK model, where $k_z = 0$. Figures 2(a)–2(c) show the angle dependence of the superconducting gap magnitude. It is obvious from these plots that all three are nodeless. Note that OPs of the s wave, (a), and A_{1u} pairing, (b), differ in their angle dependence of the phase, rather than gap magnitude. Figures 2(d)–2(f) show the normalized conductance as a function of the angle with respect to the interface normal. Brighter colors indicate a higher conductance in these graphs. Both the A_{1u} and the $E_{u(1,0)}$ pairing exhibit helical edge states within the superconducting gap. The panels labeled (g)–(i) show the calculated conductance spectra for dimensionless barrier strength $Z = 0$, 0.5, 1, and 4. The legend is included in panel (i). These dI/dV spectra are the result of angle averaging over a semicircle directed at the interface. It should be noted that no signs of unconventional superconductivity have been found in differential conductance measurements along the c axis, which rules out three-dimensional isotropic A_{1u} pairing but leaves room for an anisotropic variant [12,14]. The other nodeless pairing symmetry, $E_{u(1,0)}$, consists of components that are linear in k and cubic in k, i.e., p-wave + f-wave symmetry. This can behave like a fully gapped system only when the k^3 component is sufficiently strong compared to the linear term. Although the $E_{u(1,0)}$ nematic $p + f$-wave state is unlikely to occur in nature, recent reports on the topological superconductor $Cu_xBi_2Se_3$ have found indications of E_u pairing symmetry [25–27].

Comparing our model to the differential conductance curves displayed in Fig. 1, it appears that only conventional s-wave pairing cannot adequately explain all our findings. Although the data obtained on the two high-resistance devices

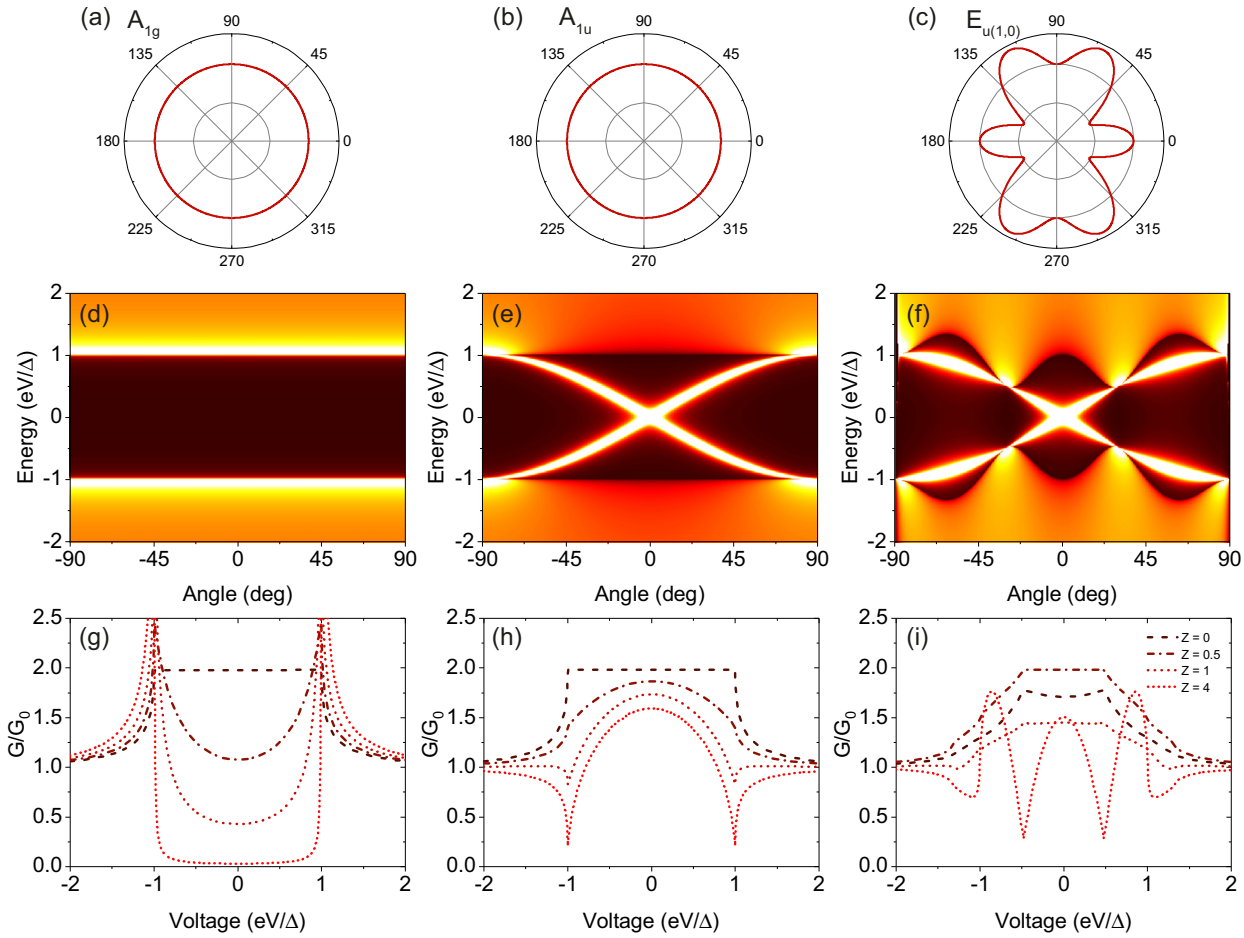

FIG. 2. The BTK model for conventional s-wave symmetry, A_{1u}, and $E_{u(1,0)}$ pairing. (a)–(c) show the angle dependence of the gap, Δ, indicating the shape of the OP and the fact that it is nodeless. (d)–(f) show the angle-dependent conductance at different energies calculated for barrier strength $Z = 4$. The colorscale reflects the conductance, where brighter colors indicate higher conductance. Both A_{1u} (e) and $E_{u(1,0)}$ (f) have helical edge states at zero energy. Note that due to the anisotropy of the $E_{u(1,0)}$ pair potential, some of the states with large k_y components on the normal metal side have no superconducting equivalent at the same energy and result in zero conductivity. (g)–(i) are the conductance spectra obtained for different dimensionless barrier strengths, Z, in the BTK model. They are the result of averaging the conductance over angles between -90° and $+90^\circ$. The legend in (i) shows which line represents which Z and is valid for (g) and (h) as well.

can be nicely replicated using s-wave pairing with some degree of broadening, the sharp dips and elevated plateau of the lower-resistance device are absent in Fig. 2(g), which shows the resulting differential conductance of the s-wave BTK model. The helical p-wave dI/dV, Fig. 2(h), does exhibit sharp dips and a rising plateau, albeit far more rounded than the experimental data. Unconventional superconductivity, as long as it is nodeless [18], is not unimaginable in $PdTe_2$ as the unique spin (or pseudo-spin) structure of a Dirac semimetal can stabilize unconventional pairing mechanisms [10,17]. However, using a combination of conventional s-wave and helical p-wave pairing, we were unable to accurately model the data of Fig. 1(a), i.e., the most transparent junction. The differential conductance of the two most resistive junctions, on the other hand, can be fitted well using only the conventional s-wave pairing model. The result of this fitting procedure is shown as a red line in Figs. 1(b) and 1(c). Every part, except for the ZBCP in Fig. 1(c) is described by the BTK model, using a dimensionless barrier strength $Z \approx 0.7$. We will leave the ZBCP for now and turn our attention to the lower R_N junctions.

To explain the origin of the sharp dips and dented plateau of Fig. 1(a) we extend our BTK model by taking into account the influence of the interfacial critical current on the obtained dI/dV spectra [20–24,28]. See Supplemental Material [29] for additional information on the model. The BTK model assumes ballistic transport through the junction at all bias voltages, but in the case of very low resistance junctions, the junction may leave the ballistic regime and enter the thermal regime: while increasing the bias current through these transparent junctions we reach the critical current I_c, an effect that comes on top of the BTK model. This critical current does not refer to the typical bulk I_c of a superconductor, but rather to a reduced critical current in the disordered surface of the $PdTe_2$ close to the interface. Upon reaching this critical current, a voltage suddenly appears across the junction, which is represented as a step in the IV characteristic. Taking the derivative of this will yield sharp dips in dI/dV at the critical current. The red line in Fig. 1(a) shows the striking agreement of an s-wave BTK model with our data, when the effect of I_c is taken into account. The BTK parameters, as well as I_c, are reported inside the graph. F describes the mixing of the

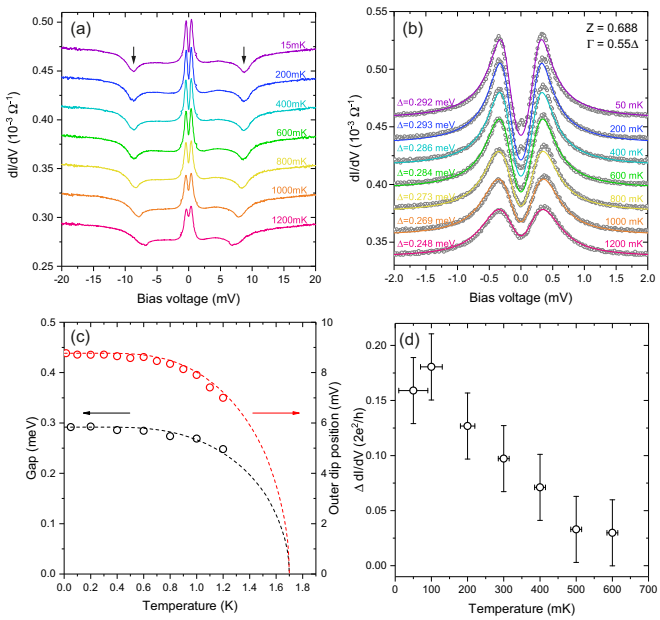

FIG. 3. Additional measurements and analysis on the highest resistance sample. (a) dI/dV of the 2.16 kΩ sample for different temperatures measured over a large range of bias voltage. For clarity, all the curves except for the 15 mK curve have been given a constant offset. (b) s-wave BTK fits (colored lines) to the measured dI/dV of the 2.16 kΩ junction (gray circles) at different temperatures. Again, all the curves except for the 15 mK curve have been given a constant offset. The temperature and fitted gap Δ are indicated next to the line. Z and Γ are shared across the curves and are indicated in the top-right corner of the graph. (c) The superconducting gap from the BTK fits as a function of temperature (black circles) and the position of the shallow dip versus temperature (red circles). Dashed lines show the standard temperature dependence from BCS theory for a T_c of 1.7 K. (d) The height of the ZBCP as a function of temperature.

I_c model and the BTK model through a linear combination, where $F = 0$ means purely BTK model and $F = 1$ is purely the I_c model. We stress that this fitting is performed using only conventional s-wave pairing, like in Fig. 1(c). The device with the largest barrier is apparently in the ballistic regime for all applied currents, whereas this does not hold for the most transparent device. The dI/dV features, occasionally ascribed to unconventional superconductivity, arise in our case from high transparency of the junction in combination with a disordered interface. This high transparency can be due to the design of the device, or an accidental feature, such as a pinhole or otherwise broken barrier. For an example of how such a dI/dV spectrum can easily be misinterpreted as originating from p-wave superconductivity see the Supplemental Material [29].

So far we have found that the main features of all three measured devices can be understood with the same OP symmetry, even though their differential conductance spectra differ greatly. The high-resistance device is our best candidate for a more extensive conductance spectroscopy study, as it exhibits ballistic transport for up to 8 mV. We have measured the dI/dV spectrum of this device at different temperatures and for a much larger range of bias currents. The experimental data is presented in Fig. 3(a). Figure 3(b) serves as a zoomed-in version of this graph around zero bias and shows, as solid lines, the curves obtained from a conventional s-wave BTK model. The theoretically obtained curves describe the data very well. A shallow dip feature presents itself in Fig. 3(a) at bias voltages greater than 5 mV, far beyond the superconducting gap (∼300 μV). The dip differs from the dips earlier attributed to the critical current. Such dips are quite sharp, since they relate to an instant increase in voltage, whereas this feature is shallow and stretched wide in voltage. Furthermore, we have plotted the position of this dip as a function of temperature in red circles in Fig. 3(c). They are accompanied by the superconducting gap Δ as extracted from the BTK fit on the low-bias part of this dataset. Both temperature dependences can be described using standard BCS theory. The two dashed lines show this standard BCS behavior, scaled to the voltage value at the lowest temperature.

Over the past decades there have been numerous experiments in which dips such as presented in Fig. 3(a) have been observed [30–32]. A possible origin of this dip is that weak spots in the barrier are responsible for the crossover into the thermal regime at larger currents, similar to our I_c model [31,32].

The final feature we discuss is the aforementioned ZBCP. This peak can clearly be distinguished in the low-bias region of the low-transparency device at sufficiently low temperatures. We have subtracted the BTK fits shown in Fig. 3(b) from the respective data and tracked the height of this peak as a function of temperature. The extracted peak heights are shown in Fig. 3(d). We see that the temperature dependence of the ZBCP is linear and the temperature at which the peak appears is much lower than the reported critical temperature of $PdTe_2$. At these temperatures the thermal energy, k_BT, is smaller than the width of the ZBCP, which hints that we are probing a different characteristic energy scale here. Recent studies of the superconductivity of $PdTe_2$ have confirmed the existence of multiple superconducting channels, related to parallel bulk and surface superconductivity [11]. Because only one device of the third type was fabricated, it is unclear whether the ZBCP arises from intrinsic superconducting properties, or from interface effects inside this specific device.

IV. CONCLUSION

In short, we have fabricated three $PdTe_2$/normal metal side junctions with different transparencies. The shape of the conductance spectra heavily depends on the normal state resistance of the junction and can make conventional superconductivity look unconventional. One should exert caution in analyzing the data of low-resistance SN junctions and confirm that the junction is solely in the ballistic limit, or include the effect of the critical current on the dI/dV spectrum in one's model. Taking these critical current effects into account in the data analysis, the conductance spectroscopy measurements on our devices indicate that the order parameter in $PdTe_2$ is dominated by conventional s-wave pairing.

ACKNOWLEDGMENTS

This work was financially supported by the European Research Council (ERC) through a Consolidator. T.H. is supported by the JSPS KAKENHI (No. JP15H05855).

[1] L. Fu and C. L. Kane, Phys. Rev. Lett. **100**, 096407 (2008).

[2] S. Das Sarma, M. Freedman, and C. Nayak, npj Quant. Inf. **1**, 15001 (2015).

[3] V. Mourik, K. Zuo, S. M. Frolov, S. R. Plissard, E. P. A. M. Bakkers, and L. P. Kouwenhoven, Science **336**, 1003 (2012).

[4] L. P. Rokhinson, X. Liu, and J. K. Furdyna, Nat. Phys. **8**, 795 (2012).

[5] J. Wiedenmann, E. Bocquillon, R. S. Deacon, S. Hartinger, O. Herrmann, T. M. Klapwijk, L. Maier, C. Ames, C. Brüne, C. Gould, A. Oiwa, K. Ishibashi, S. Tarucha, H. Buhmann, and L. W. Molenkamp, Nat. Commun. **7**, 10303 (2016).

[6] H.-H. Sun, K.-W. Zhang, L.-H. Hu, C. Li, G.-Y. Wang, H.-Y. Ma, Z.-A. Xu, C.-L. Gao, D.-D. Guan, Y.-Y. Li, C. Liu, D. Qian, Y. Zhou, L. Fu, S.-C. Li, F.-C. Zhang, and J.-F. Jia, Phys. Rev. Lett. **116**, 257003 (2016).

[7] M. Snelder, M. Veldhorst, A. A. Golubov, and A. Brinkman, Phys. Rev. B **87**, 104507 (2013).

[8] C. Li, J. C. de Boer, B. de Ronde, S. V. Ramankutty, E. van Heumen, Y. Huang, A. de Visser, A. A. Golubov, M. S. Golden, and A. Brinkman, Nat. Mater. **17**, 875 (2018).

[9] S. Sasaki, M. Kriener, K. Segawa, K. Yada, Y. Tanaka, M. Sato, and Y. Ando, Phys. Rev. Lett. **107**, 217001 (2011).

[10] L. Fu and E. Berg, Phys. Rev. Lett. **105**, 097001 (2010).

[11] H. Leng, C. Paulsen, Y. K. Huang, and A. de Visser, Phys. Rev. B **96**, 220506(R) (2017).

[12] S. Das, Amit, A. Sirohi, L. Yadav, S. Gayen, Y. Singh, and G. Sheet, Phys. Rev. B **97**, 014523 (2018).

[13] Amit and Y. Singh, Phys. Rev. B **97**, 054515 (2018).

[14] O. J. Clark, M. J. Neat, K. Okawa, L. Bawden, I. Marković, F. Mazzola, J. Feng, V. Sunko, J. M. Riley, W. Meevasana, J. Fujii, I. Vobornik, T. K. Kim, M. Hoesch, T. Sasagawa, P. Wahl, M. S. Bahramy, and P. D. C. King, Phys. Rev. Lett. **120**, 156401 (2018).

[15] H.-J. Noh, J. Jeong, E.-J. Cho, K. Kim, B. I. Min, and B.-G. Park, Phys. Rev. Lett. **119**, 016401 (2017).

[16] Y. Liu, J. Zhao, L. Yu, C. Lin, C. Hu, D. Liu, Y. Peng, Z. Xie, J. He, C. Chen, Y. feng, H. Yi, X. Liu, L. Zhao, S. He, G. Liu, X. Dong, J. Zhang, C. Chen, Z. Xu, H. Weng, X. Dai, Z. Fang, and X. J. Zhou, Chin. Phys. B **24**, 067401 (2015).

[17] M. Sato and Y. Ando, Rep. Prog. Phys. **80**, 076501 (2017).

[18] S. Teknowijoyo, N. H. Jo, M. S. Scheurer, M. A. Tanatar, K. Cho, S. L. Bud'ko, P. P. Orth, P. C. Canfield, and R. Prozorov, Phys. Rev. B **98**, 024508 (2018).

[19] G. E. Blonder, M. Tinkham, and T. M. Klapwijk, Phys. Rev. B **25**, 4515 (1982).

[20] G. Sheet, S. Mukhopadhyay, and P. Raychaudhuri, Phys. Rev. B **69**, 134507 (2004).

[21] V. Baltz, A. D. Naylor, K. M. Seemann, W. Elder, S. Sheen, K. Westerholt, H. Zabel, G. Burnell, C. H. Marrows, and B. J. Hickey, J. Phys.: Condens. Matter **21**, 095701 (2009).

[22] D. Daghero and R. S. Gonnelli, Supercond. Sci. Technol. **23**, 043001 (2010).

[23] Yu. G. Naidyuk, and K. Gloos, Low Temp. Phys. **44**, 257 (2018).

[24] R. Taboryski, T. Clausen, J. Bindslev Hansen, J. L. Skov, J. Kutchinsky, C. B. Sørensen, and P. E. Lindelof, Appl. Phys. Lett. **69**, 656 (1996).

[25] K. Matano, M. Kriener, K. Segawa, Y. Ando, and G.-q. Zheng, Nat. Phys. **12**, 852 (2016).

[26] T. Hashimoto, K. Yada, A. Yamakage, M. Sato, and Y. Tanaka, J. Phys. Soc. Jpn. **82**, 044704 (2013).

[27] S. Yonezawa, K. Tajiri, S. Nakata, Y. Nagai, Z. Wang, K. Segawa, Y. Ando, and Y. Maeno, Nat. Phys. **13**, 123 (2017).

[28] B. I. Verkin, I. K. Yanson, I. O. Kulik, O. I. Shklyarevski, A. A. Lysykh, and Yu. G. Naydyuk, Solid State Commun. **30**, 215 (1979).

[29] See Supplemental Material at http://link.aps.org/supplemental/10.1103/PhysRevB.99.014510 for additional information regarding the I_c + BTK model and an example of its similarity to a p-wave BTK spectrum.

[30] C. Nguyen, H. Kroemer, and E. L. Hu, Phys. Rev. Lett. **69**, 2847 (1992).

[31] P. Raychaudhuri, D. Jaiswal-Nagar, G. Sheet, S. Ramakrishnan, and H. Takeya, Phys. Rev. Lett. **93**, 156802 (2004) (Supplemental Material).

[32] D. L. Bashlakov, Yu. G. Naidyuk, I. K. Yanson, S. C. Wimbush, B. Holzapfel, G. Fusch, and S.-L. Drechsler, Supercond. Sci. Technol. **18**, 1094 (2005).